

Hierarchical Feature-level Reverse Propagation for Post-Training Neural Networks

Ni Ding^{2,3} Lei He^{1,2, *} Shengbo Eben Li^{1,2} Keqiang Li^{1,2}

Abstract

End-to-end autonomous driving has emerged as a dominant paradigm, yet its highly entangled black-box models pose significant challenges in terms of interpretability and safety assurance. To improve model transparency and training flexibility, this paper proposes a hierarchical and decoupled post-training framework tailored for pretrained neural networks. By reconstructing intermediate feature maps from ground-truth labels, surrogate supervisory signals are introduced at transitional layers to enable independent training of specific components, thereby avoiding the complexity and coupling of conventional end-to-end backpropagation and providing interpretable insights into networks' internal mechanisms. To the best of our knowledge, this is the first method to formalize feature-level reverse computation as well-posed optimization problems, which we rigorously reformulate as systems of linear equations or least squares problems. This establishes a novel and efficient training paradigm that extends gradient backpropagation to feature backpropagation. Extensive experiments on multiple standard image classification benchmarks demonstrate that the proposed method achieves superior generalization performance and computational efficiency compared to traditional training approaches, validating its effectiveness and potential.

Keywords: hierarchical and decoupled post-train, explainable AI, feature map reconstruction, autonomous driving.

1 Introduction

As a rapidly advancing technology in recent years, artificial intelligence (AI) based on deep neural networks (DNNs) [19] provides promising solutions for autonomous driving (AD). Featured in optimizing all processing steps simultaneously, end-to-end (E2E) models that directly map raw sensor inputs to driving commands [4, 8, 27, 30, 38] have become the dominant paradigm in AD systems for their remarkable performance. However, the inherent opacity of DNNs presents a significant barrier to safety assurance, which can be further exacerbated in highly complex AD pipelines [6, 16]. Additionally, despite the effectiveness of jointly optimizing E2E models, training a high-performing and trustworthy AD model can be data-intensive and computationally expensive, thereby necessitating more explainable and more scalable approaches.

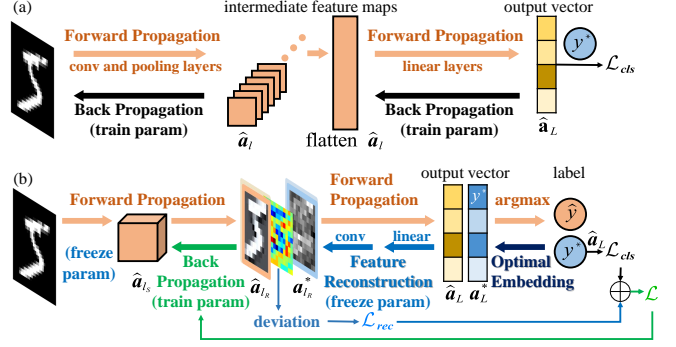


Figure 1: (a) Conventional back propagation training approach on CNN for image classification tasks. (b) Our hierarchical and decoupled post-training framework based on feature map reconstruction for image classification tasks.

On the contrary, the modularization paradigm comprises a sequence of refined components for distinct subtasks such as object detection, trajectory prediction, and route planning. Modular architectures allow engineering teams to independently make improvements on specialized modules [27], and are generally more transparent than seamless E2E models as self-contained modules can expose some intermediate information [16]. For instance, BEVFormer V2 [31], CLIP-BEVFormer [21], DiffStack [12], ChauffeurNet [2] and the 3D detector with pixel-wise depth prediction loss [13] use intermediate outputs of specific modules as auxiliary loss terms to promote optimization. In well-defined perception modules, some transitional results can be explained post-hoc by visualizing attribution heatmaps [15, 23, 33].

With the vision of integrating both conceptions, this study develops a modularization evaluation and a hierarchical decoupled post-training framework for E2E architectures (Fig.1), aiming to enhance explainability and enable targeted optimization while retaining the superior performance of E2E models.

Considering their essential role in AD applications, this paper focuses on image classification tasks. Fig.2 illustrates that certain intermediate layers in a converged convolutional neural network (CNN) are independently post-trained, while the remaining modules are kept frozen. Specifically, the feature maps \mathbf{a}_l^* , $l \in \{L, L-1, \dots, l_R\}$ are constructed layer by layer using the proposed optimal embedding algorithm (OE) and the feature reconstruction algorithms (FR), and the feature map \mathbf{a}_l^* serves as the surrogate signal of the ground truth label y^* at l_R^{th} layer. The OE part seeks the reconstructed output vector \mathbf{a}_L^* that is closest to the original forward output vector $\hat{\mathbf{a}}_L$ and satisfies $y^* = \arg \max_i (\mathbf{a}_L^*)_i$, which we managed to find the

*Corresponding author: helei2023@tsinghua.edu.cn

¹School of Vehicle and Mobility, Tsinghua University, Beijing 100084, China.

²State Key Laboratory of Intelligent Green Vehicle and Mobility, Tsinghua University, Beijing 100084, China.

³School of Mathematics and Statistics, Beijing Institute of Technology, Beijing 100081, China.

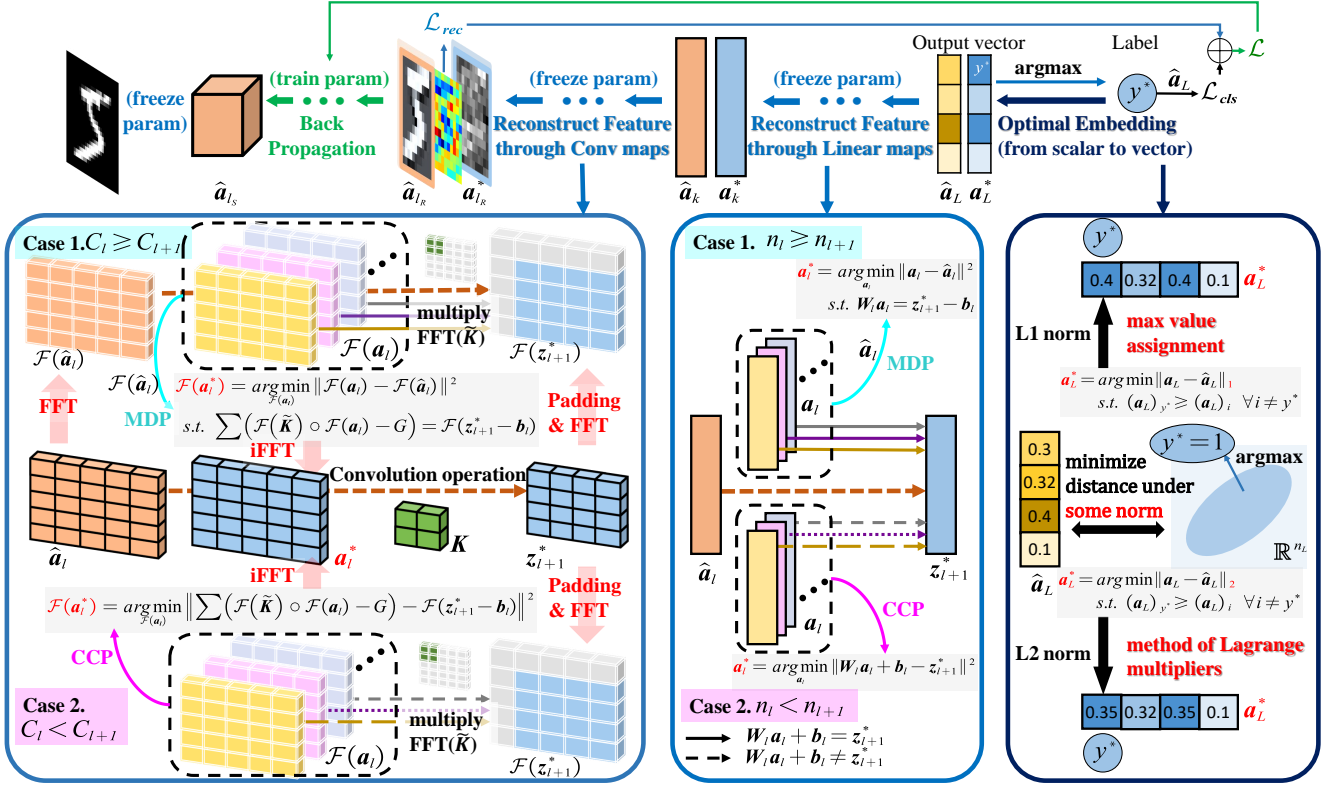


Figure 2: **Hierarchical and Decoupled Post-Training based on Feature Map Reconstruction for Image Classification Tasks.** Given a well-trained CNN, the optimal embedding and feature reconstruction are executed in line with the network’s backward computation flow to obtain the reconstructed (l_R)th feature map. A combination of reconstruction loss and classification loss is then used to post-train the intermediate modules from l_S^{th} layer to l_R^{th} layer.

optimum solution under L1 norm and L2 norm respectively. Then FR through linear or convolutional operations are executed layer by layer until achieving the $\mathbf{a}_{l_R}^*$. The FR processes are modeled as two types of optimization problems depending on whether the channel number C_l (or vector dimension n_l) of the l^{th} feature map is greater than the channel number C_{l+1} (or vector dimension n_{l+1}) of the $(l+1)^{th}$ feature map or not. This dichotomy results from whether the desired $\mathbf{a}_{l_R}^*$ that satisfies network computation, is underdetermined (infinitely many solutions) or overdetermined (no exact solution). Subsequently, the deviation between the forward feature $\hat{\mathbf{a}}_{l_R}$ and the reconstructed feature $\mathbf{a}_{l_R}^*$ is defined as the reconstruction loss \mathcal{L}_{rec} . Modules from l_S^{th} layer to l_R^{th} layer are optimized via back propagation (BP) using a combination of \mathcal{L}_{rec} and the final classification loss \mathcal{L}_{cls} .

Our contributions can be summarized as follows.

- We originally propose a post-training approach on the basis of FR-backpropagation to achieve targeted optimization, which also provides a novel feature map deviation visualization method to encourage explainability.
- The FR algorithm for linear operations is skillfully designed. Guided by optimization theory, solving a systems of linear equations or a least squares problem constitutes the majority of computation in this FR process.
- Informed by the FR for linear operations, the FR for con-

volutional operations is meticulously formalized, additionally leveraging fast Fourier transform (FFT) to substantially reduce computational cost.

- The optimal embedding that maps category labels to reconstructed output vectors is systematically discussed, and its precise optimum solutions under the L1 and L2 norm can be obtained efficiently.

2 Related Work

2.1 Decoupling Networks

Decoupled learning has been widely researched to address inefficiencies of lockings in BP approaches. Jaderberg et al. [9] developed decoupled neural interfaces, where synthetic gradients are used to decouple layer updates, allowing for asynchronous training of different modules. As a simpler yet more parallelizable alternative, decoupled greedy learning based on a greedy relaxation of the joint learning objective was later introduced [3]. Similarly, Zhuang et al. [40] explored delayed gradient updates to achieve a fully decoupled training scheme that can train modules independently, reducing memory overhead while maintaining competitive performance. Peng et al. [22] extended decoupled learning by incorporating re-computation and weight prediction strategies to mitigate memory explosion.

Beyond decoupled training, several works have partially decoupled deep networks by extracting comprehensible knowledge or instructive information for the purpose of improving interpretability. Li et al. [17] proposed Ego-Net to better estimate egocentric vehicle orientation by extracting meaningful intermediate geometrical representations. Odense and Garcez [20] proposed a layer-wise extraction method using M-of-N rules, demonstrating considerable explanations for certain layers, such as softmax layers. Furthermore, Zhang et al. [36] managed to train a feature map convergence evaluation network to quantitatively assess the training maturity of individual modules.

2.2 Explainable AI for AD systems

Over the past few years, researchers have extensively explored visualization methods to help understanding DNN outputs in classification or perception tasks. Class activation mapping (CAM), introduced by Zhou et al. [39], highlights class-specific influential regions to explain model decisions. Simonyan et al. [26] proposed gradient-based visualization methods for class saliency maps across various CNNs. This work laid the foundation for Grad-CAM [25], an extension version of CAM introduced by Selvaraju et al. Besides, Jiang et al. [10] further advanced this by proposing LayerCAM, which integrates hierarchical class activation maps to refine localization accuracy. Furthermore, Shapley value-based CAM [37] obtains the importance of each pixel through the Shapley values. Zeiler and Fergus [35] introduced a deconvolutional network to project feature activations back to the input pixel space, giving insight into the function of intermediate feature layers. OD-XAI [18] utilized Grad-CAM and saliency maps to locate the important regions that contribute to semantic road segmentation. Abukmeil et al. [1] proposed the first explainable semantic segmentation model for AD based on the variational autoencoder, which used multiscale second-order derivatives between the latent space and the encoder layers to capture the curvatures of the neurons' responses. For LiDAR-based 3D object detection, OccAM's Laser [24] serves as a perturbation-based approach empirically estimates the importance of each point by testing the model with randomly generated subsets of the input point cloud without requiring any prior knowledge of model architectures or parameters. Gou et al. [7] developed a visual analytics system equipped with a disentangled representation learning and semantic adversarial learning, to assess, understand, and improve traffic light detection. Moreover, interactive software that allows real-time inspection of neuron activations, and a high-quality feature visualization method via regularized optimization are helpful in inspiring intuition [34].

Regarding planning and prediction tasks, the generated explanations rely on attention mechanisms either as part of the transformer architecture or in conjunction with a recurrent neural network (RNN) [16]. Jiang et al. [11] proposed an intention-aware interactive transformer model to address the problem of real-time vehicle trajectory prediction in large-scale dense traffic scenarios. Kochakarn et al. [14] proposed a self-supervision pipeline with the attention mechanisms that can create spatial and temporal heatmaps on the scene graphs, to infer representative and well-separated embeddings. Wang

et al. [28] presented a method for intention prediction of surrounding vehicles using a bidirectional long short term memory network combined with a conditional random field layer, which can find the characteristics that contribute the most to the prediction.

These state-of-the-art techniques greatly improve the explainability of AI in AD tasks and can be deployed into existing decision-making systems [16]. However, they still face the sharp trade-off between computational overhead and performance, since the interpretation monitor is supposed to not take too much time to operate [32]. In addition, these explainable algorithms may fail to correctly capture the crucial attributes that are responsible for degraded outputs due to their modeling defects [16].

3 Method

Consider a pretrained baseline CNN with its weight \mathbf{W}_l and bias \mathbf{b}_l for each l^{th} layer, $l \in \{1, 2, \dots, L\}$. Denote the l^{th} preactivated feature by $\hat{\mathbf{z}}_l$, and the l^{th} activated feature by $\hat{\mathbf{a}}_l = \text{activate}(\mathbf{z}_l)$, which satisfies $\hat{\mathbf{z}}_{l+1} = \mathbf{W}_l \hat{\mathbf{a}}_l + \mathbf{b}_l$. In general, we assume that the linear weight matrix \mathbf{W}_l is always full-rank in all subsequent analyses.

The post-train of the modules from the l_S^{th} layer to the l_R^{th} layer can be performed by optimizing the following loss \mathcal{L} , where the core and crux of FR-PT lies in how to reconstruct the feature maps $\mathbf{a}_{l_R}^*$ from final labels appropriately and efficiently.

$$\mathcal{L}_{cls} = \text{CrossEntropy}(\mathbf{y}^*, \hat{\mathbf{a}}_L) \quad (1)$$

$$\mathcal{L}_{rec} = \text{MSE}(\mathbf{a}_{l_R}^*, \hat{\mathbf{a}}_{l_R}) \quad (2)$$

$$\mathcal{L} = (1 - \alpha)\mathcal{L}_{cls} + \alpha\mathcal{L}_{rec} \quad (3)$$

We adopt a greedy strategy to reconstruct all feature maps from \mathbf{a}_L^* to $\mathbf{a}_{l_R}^*$ layer by layer. That is, each reconstruction step from \mathbf{z}_{l+1}^* and parameters at the l^{th} layer, pursues the "best" \mathbf{a}_l^* without considering other feature maps, resulting in the obtained \mathbf{a}_l^* may not be the optimal choice for successive determinations of feature maps \mathbf{a}_k^* , where $k < l$.

Since multiple operations are commonly involved in CNNs, we divide them into linear operations, convolutional operations, the "argmax" operation, and other operations in the following discussion. Before giving concrete algorithms, we need to analyze the reverse computation of linear operations at the single l^{th} layer. During the transformation from $\hat{\mathbf{a}}_l$ to $\hat{\mathbf{z}}_{l+1}$, the feature channels either expand or contract, which makes the linear system $\mathbf{W}_l \mathbf{a}_l^* + \mathbf{b}_l = \mathbf{z}_{l+1}^*$ either unsolvable or underdetermined, respectively. In order to cope with the first case, the computing consistency principle (CCP) is proposed to determine the feature \mathbf{a}_l^* that minimizes the computing consistency error $\|\mathbf{W}_l \mathbf{a}_l^* + \mathbf{b}_l - \mathbf{z}_{l+1}^*\|$ as the reconstructed feature. In regard of the second case, the minimal deviation principle (MDP) is proposed to prefer the feature \mathbf{a}_l^* that minimizes the deviation degree $\|\mathbf{a}_l^* - \hat{\mathbf{a}}_l\|$ among all features that satisfy the linear computation $\mathbf{W}_l \mathbf{a}_l^* + \mathbf{b}_l = \mathbf{z}_{l+1}^*$, as the reconstructed feature. Both principles choose the feature \mathbf{a}_l^* in a way that can mostly inherit the superiority capability of former converged network computation, that is, leverage the exceptional achievement of E2E overall optimization.

3.1 Feature Reconstruction through Linear Operations

Given the reconstructed $(l+1)^{th}$ preactivation feature map \mathbf{z}_{l+1}^* with dimension n_{l+1} , the frozen linear weights \mathbf{W}_l , bias \mathbf{b}_l , and the original l^{th} activated feature $\hat{\mathbf{a}}_l$ with dimension n_l , the reconstructed l^{th} activated feature \mathbf{a}_l^* is desired. Adhere to the architecture of the baseline CNN, one can choose either of the following cases to perform.

(a) $n_l \geq n_{l+1}$. Among the infinitely many solutions \mathbf{a}_l satisfying $\mathbf{W}_l \mathbf{a}_l + \mathbf{b}_l = \mathbf{z}_{l+1}^*$, the one closest to the original version $\hat{\mathbf{a}}_l$ is preferred as the reconstructed feature \mathbf{a}_l^* according to MDP. For each instance x , Eq. 4 provides a strict convex quadratic programming with linear constraints.

$$\begin{aligned} \mathbf{a}_l^* &= \arg \min_{\mathbf{a}_l} \|\mathbf{a}_l - \hat{\mathbf{a}}_l\|^2 \\ \text{s.t. } & \mathbf{W}_l \mathbf{a}_l = \mathbf{z}_{l+1}^* - \mathbf{b}_l \end{aligned} \quad (4)$$

Dual method [5] is applied to solve Eq. 4. The Lagrangian function is $L(\mathbf{a}_l, \boldsymbol{\lambda}) = \|\mathbf{a}_l - \hat{\mathbf{a}}_l\|^2 - \boldsymbol{\lambda}(\hat{\mathbf{a}}_l \mathbf{W}_l + \mathbf{b}_l - \mathbf{z}_{l+1}^*)$, where $\boldsymbol{\lambda} \in \mathbb{R}^{n_{l+1}}$ is the Lagrange multiplier. Set its partial derivative to zero as Eq. 5.

$$\frac{\partial L}{\partial \mathbf{a}_l}(\mathbf{a}_l^*, \boldsymbol{\lambda}^*) = \mathbf{0}, \quad \frac{\partial L}{\partial \boldsymbol{\lambda}}(\mathbf{a}_l^*, \boldsymbol{\lambda}^*) = \mathbf{0} \quad (5)$$

Write these two equations in $(n_l + n_{l+1})$ -dimensional matrix form as Eq. 6.

$$\begin{pmatrix} 2\mathbb{I}_{n_l} & -\mathbf{W}_l^T \\ \mathbf{W}_l & \mathbf{0}_{n_{l+1}} \end{pmatrix} \begin{pmatrix} \mathbf{a}_l^* \\ \boldsymbol{\lambda}^* \end{pmatrix} = \begin{pmatrix} 2\hat{\mathbf{a}}_l \\ \mathbf{z}_{l+1}^* - \mathbf{b}_l \end{pmatrix}, \forall x \quad (6)$$

Since \mathbf{W}_l is full-rank matrix, the left matrix is full-rank, suggesting that there exists a unique solution $(\mathbf{a}_l^*, \boldsymbol{\lambda}^*) \in \mathbb{R}^{n_l + n_{l+1}}$.

(b) $n_l < n_{l+1}$. The \mathbf{a}_l^* with minimal squared error of the computing consistency is pursued, thereby yielding for a least squares problem 7.

$$\mathbf{a}_l^* = \arg \min_{\mathbf{a}_l} \|\mathbf{W}_l \mathbf{a}_l + \mathbf{b}_l - \mathbf{z}_{l+1}^*\|^2, \forall x \quad (7)$$

Both the system of linear equations 6 and the least squares problem 7 have been well-studied, and can be solved efficiently using standard numerical methods.

3.2 Feature Reconstruction through Convolutional Operations

Given the reconstructed $(l+1)^{th}$ pre-activated feature $\mathbf{z}_{l+1}^* \in \mathbb{R}^{BS \times C_{l+1} \times H_{l+1} \times W_{l+1}}$, the frozen convolutional kernel \mathbf{K}_l , bias \mathbf{b}_l , and the original l^{th} activated feature map $\hat{\mathbf{a}}_l \in \mathbb{R}^{BS \times C_l \times H_l \times W_l}$, the reconstructed l^{th} activated feature \mathbf{a}_l^* is desired. For engineering convenience, this study focuses primarily on the case where the convolutional kernels use stride 1 and no padding (i.e., $\text{stride} = 1, \text{padding} = 0$). Under this setting, the feature map sizes satisfy $H_l > H_{l+1}$ and $W_l > W_{l+1}$.

As a variety of linear transformation, the reconstruction of convolutional operation can be solved by formulae in Section

3.1. However, due to the larger feature map size and the multiplexing of convolutional kernels \mathbf{K}_l , this method can be highly computationally expensive. To deal with this, we designed an algorithm based on FFT and convolution theorem to significantly reduce computing complexity while causing negligible additional modeling error.

Let $T_{n,m}^x$ be the contribution from the m^{th} channel of feature map $\hat{\mathbf{a}}_l$ to the n^{th} channel of feature map $\hat{\mathbf{z}}_{l+1}$ for instance x . The “ \otimes ” in Eq. 8 implies convolutional operation in neural networks.

$$T_{n,m}^x = \hat{\mathbf{a}}_l[x, m] \otimes \mathbf{K}[n, m] \in \mathbb{R}^{H_{l+1} \times W_{l+1}} \quad (8)$$

Thus, the n^{th} channel of $\hat{\mathbf{z}}_{l+1}$ for instance x is given by Eq. 9.

$$\hat{\mathbf{z}}_{l+1}[x, n] = \sum_{m=1}^{C_l} T_{n,m}^x + (\mathbf{b}_l)_n \quad (9)$$

To utilize the convolution theorem, $\mathcal{F}(f)\mathcal{F}(g) = \mathcal{F}(f * g)$, the operation in convolutional layer “ \otimes ” needs to be replaced by convolution in mathematical version “ $*$ ”. Thus the original convolutional kernel \mathbf{K} needs to be flipped as the following $\tilde{\mathbf{K}} \in \mathbb{R}^{H_{\mathbf{K}} \times W_{\mathbf{K}}}$.

$$\tilde{\mathbf{K}}[n, m](s, t) = \mathbf{K}[n, m](H_{\mathbf{K}} - 1 - s, W_{\mathbf{K}} - 1 - t) \quad (10)$$

Hence, we have formula 11. Note that the “ $*$ ” here is not standard mathematical notation for convolution in neural networks do not regard tensors as functions on infinite spaces, which means the boundary needs further processing.

$$\begin{aligned} T_{n,m}^x(i, j) &= \sum_{s=1}^{H_{\mathbf{K}}} \sum_{t=1}^{W_{\mathbf{K}}} \hat{\mathbf{a}}_l[x, m](i + s, j + t) \mathbf{K}[n, m](s, t) \\ &= \sum_{s'=1}^{H_{\mathbf{K}}} \sum_{t'=1}^{W_{\mathbf{K}}} \hat{\mathbf{a}}_l[x, m](i + H_{\mathbf{K}} - 1 - s', j + W_{\mathbf{K}} - 1 - t') \cdot \\ &\quad \tilde{\mathbf{K}}[n, m](s', t') \\ &= \hat{\mathbf{a}}_l[x, m] * \tilde{\mathbf{K}}[n, m] \in \mathbb{R}^{H_{l+1} \times W_{l+1}} \end{aligned} \quad (11)$$

The Fourier transforms of $\tilde{\mathbf{K}}[n, m]$, $\hat{\mathbf{a}}_l[x, m]$, and $T_{n,m}^x$ are Eq. 12, 13, and 14, respectively, where i refers to the imaginary unit. With the goal to preserve all information, we zero-pad $T_{n,m}^x$ on the left and top, and $\tilde{\mathbf{K}}[n, m]$ on the right and bottom, so as to make $\mathcal{F}(\tilde{\mathbf{K}}[n, m])$ and $\mathcal{F}(T_{n,m}^x)$ match the shape of $\mathcal{F}(\hat{\mathbf{a}}_l[x, m])$.

$$\mathcal{F}(\tilde{\mathbf{K}}[n, m])(u, v) = \sum_{s=1}^{H_{\mathbf{K}}} \sum_{t=1}^{W_{\mathbf{K}}} \tilde{\mathbf{K}}[n, m](s, t) e^{-2\pi i (\frac{us}{H_l} + \frac{vt}{W_l})} \quad (12)$$

$$\mathcal{F}(\hat{\mathbf{a}}_l[x, m])(u, v) = \sum_{k=1}^{H_l} \sum_{j=1}^{W_l} \hat{\mathbf{a}}_l[x, m](k, j) e^{-2\pi i (\frac{uk}{H_l} + \frac{vj}{W_l})} \quad (13)$$

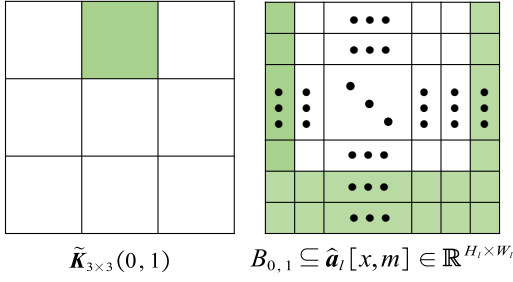


Figure 3: Schematic diagram of the boundary set $B_{0,1}$ for $\tilde{\mathbf{K}}(0, 1)$.

$$\begin{aligned}
 & \mathcal{F}(T_{n,m}^x)(u, v) \\
 &= \sum_{k=1}^{H_{l+1}} \sum_{j=1}^{W_{l+1}} T_m^{b,n}(k, j) e^{-2\pi i \left(\frac{u(k+H_{\mathbf{K}}-1)}{H_l} + \frac{v(j+W_{\mathbf{K}}-1)}{W_l} \right)} \\
 &= \sum_{k=1}^{H_{l+1}} \sum_{j=1}^{W_{l+1}} \sum_{s=1}^{H_{\mathbf{K}}} \sum_{t=1}^{W_{\mathbf{K}}} \hat{\mathbf{a}}_l[x, m](k+H_{\mathbf{K}}-1-s, j+W_{\mathbf{K}}-1-t) \cdot \\
 & \quad \tilde{\mathbf{K}}[n, m](s, t) e^{-2\pi i \left(\frac{u(k+H_{\mathbf{K}}-1)}{H_l} + \frac{v(j+W_{\mathbf{K}}-1)}{W_l} \right)} \quad (14)
 \end{aligned}$$

Due to the finiteness of feature map size, the boundary of feature maps needs further modification using Eq. 15, where set $B_{s,t}$ for each $(s, t) \in H_{\mathbf{K}} \times W_{\mathbf{K}}$ contains all boundary elements in $\hat{\mathbf{a}}_l$ that $T_{n,m}^x$ does not count while $\mathcal{F}(\hat{\mathbf{a}}_l[x, m]) \circ \mathcal{F}(\tilde{\mathbf{K}}[n, m])$ does, as shown in Fig.3.

$$\begin{aligned}
 G_{n,m}^x[\hat{\mathbf{a}}_l[x, m]](u, v) &= \sum_{s=1}^{H_{\mathbf{K}}} \sum_{t=1}^{W_{\mathbf{K}}} \sum_{(k,j) \in B_{s,t}} \tilde{\mathbf{K}}[n, m](s, t) \cdot \\
 & \quad \hat{\mathbf{a}}_l[x, m](k, j) e^{-2\pi i \left(\frac{u(s+k)}{H_l} + \frac{v(t+j)}{W_l} \right)} \quad (15)
 \end{aligned}$$

Thereupon, one can verify the network computing $\mathbf{a}_l^*[x, m] \otimes \mathbf{K}[n, m] = T_{n,m}^x[\mathbf{a}_l^*]$ is equivalent to equation 16, where "o" is element-wise multiplication.

$$\mathcal{F}(\mathbf{a}_l^*[x, m]) \circ \mathcal{F}(\tilde{\mathbf{K}}[n, m]) - G_{n,m}^x[\mathbf{a}_l^*] = \mathcal{F}(T_{n,m}^x[\mathbf{a}_l^*]) \quad (16)$$

Since Fourier transform is linear, the desired newtork computation (Eq. 9) is equivalent to Eq. 17 for any $n \in C_{l+1}$ and any instance x .

$$\begin{aligned}
 \mathcal{F}(\mathbf{z}_{l+1}^*[x, n] - (\mathbf{b}_l)_n) &= \sum_{m=1}^{C_l} \mathcal{F}(T_{n,m}^x[\mathbf{a}_l^*]) \\
 &= \sum_{m=1}^{C_l} \{ \mathcal{F}(\mathbf{a}_l^*[x, m]) \circ \mathcal{F}(\tilde{\mathbf{K}}[n, m]) - G_{n,m}^x[\mathbf{a}_l^*] \} \quad (17)
 \end{aligned}$$

In real computing, the $G_{n,m}^x[\mathbf{a}_l^*]$ is replaced by $G_{n,m}^x[\hat{\mathbf{a}}_l]$, leading formula 17 to be approximately correct.

(a) $C_l \geq C_{l+1}$. We need to solve a convex quadratic programming 18 established by the MDP, for each $(u, v) \in$

$H_l \times W_l$ and each instance x .

$$\begin{aligned}
 & \min_{\mathcal{F}(\mathbf{a}_l[x, m])} \sum_{m=1}^{C_l} \|\mathcal{F}(\mathbf{a}_l[x, m])(u, v) - \mathcal{F}(\hat{\mathbf{a}}_l[x, m])(u, v)\|^2 \\
 & \text{s.t.} \quad \sum_{m=1}^{C_l} (\mathcal{F}(\mathbf{a}_l[x, m]) \circ \mathcal{F}(\tilde{\mathbf{K}}[n, m]) - G_{n,m}^x[\hat{\mathbf{a}}_l])(u, v) \\
 & \quad = \mathcal{F}(\mathbf{z}_{l+1}^*[x, n] - (\mathbf{b}_l)_n)(u, v), n = 1, 2, \dots, C_{l+1} \quad (18)
 \end{aligned}$$

According to Eq. 6, the linear system 19 can be built for each $(u, v) \in H_l \times W_l$ and each instance x , producing the $\mathcal{F}(\mathbf{a}_l^*[x, m])(u, v), m = 1, 2, \dots, C_l$ each time.

$$\begin{pmatrix} \mathbb{I}_{C_l} & \mathcal{F}(\tilde{\mathbf{K}})^T \\ \mathcal{F}(\tilde{\mathbf{K}}) & \mathbf{0}_{C_{l+1}} \end{pmatrix} \begin{pmatrix} \mathcal{F}(\mathbf{a}_l^*) \\ -\frac{1}{2} \lambda^* \end{pmatrix} = \begin{pmatrix} \mathcal{F}(\hat{\mathbf{a}}_l) \\ \mathcal{F}(\mathbf{z}_{l+1}^* - (\mathbf{b}_l)_n) + \sum_{m=1}^{C_l} G_{n,m}^x \end{pmatrix} \quad (19)$$

(b) $C_l < C_{l+1}$. We need to solve a least square problem 20 established by the CCP, for each $(u, v) \in H_l \times W_l$ and each instance x . $\mathcal{F}(\mathbf{a}_l^*[x, m])(u, v), m = 1, 2, \dots, C_l$ can be obtained each time.

$$\min_{\mathcal{F}(\mathbf{a}_l)} \left\| \sum_{m=1}^{C_l} (\mathcal{F}(\tilde{\mathbf{K}}) \circ \mathcal{F}(\mathbf{a}_l) - G_{n,m}^x[\hat{\mathbf{a}}_l]) - \mathcal{F}(\mathbf{z}_{l+1}^* - (\mathbf{b}_l)_n) \right\|^2 \quad (20)$$

Finally, since Fourier transform is an isometry, i.e., it preserves distances in the L2 norm such that $\|\mathcal{F}(\mathbf{x}) - \mathcal{F}(\mathbf{y})\|_{L_2} = \|\mathbf{x} - \mathbf{y}\|_{L_2}$, the desired reconstructed feature map \mathbf{a}_l^* can be directly obtained by applying the inverse FFT to $\mathcal{F}(\mathbf{a}_l^*)$.

3.3 Optimal Embedding for Category Labels

Obviously, there are infinitely many output vector candidates whose argmax corresponds to the correct category label. According to MDP, the optimal output vector reconstruction \mathbf{a}_L^* can be seeked by solving problem 21, where $\|\cdot\|_N$ denotes some type of norm, and $(\mathbf{a}_L)_k$ denotes the k^{th} entry of vector \mathbf{a}_L . In this section, we will discuss this problem under L1 and L2 norms.

$$\min_{\mathbf{a}_L} \|\mathbf{a}_L - \hat{\mathbf{a}}_L\|_N \quad (21)$$

$$\text{s.t.} (\mathbf{a}_L)_{y^*} \geq (\mathbf{a}_L)_i, \forall i \in I_{y^*} = \{1, 2, \dots, n_L\} - \{y^*\}$$

(a). A trivial solution called "Maximum Assignment (MA)" 22, simply assigns the maximum value to the ground-truth label $(y^*)^{th}$ entry.

$$(\mathbf{a}_L^{MA})_j = \begin{cases} \max_i (\hat{\mathbf{a}}_L)_i, & \text{when } j = y^* \\ (\hat{\mathbf{a}}_L)_j, & \text{otherwise} \end{cases} \quad (22)$$

proposition: When $\|\cdot\|_N$ is set to the L1 norm, MA solution \mathbf{a}_L^{MA} is the optimal output vector reconstruction \mathbf{a}_L^* .

Proof. MA solution \mathbf{a}_L^{MA} satisfies the constraint condition in problem 21. It suffices to check whether the MA solution has the minimum norm. The L1 norm is the sum of absolute values of all entries. For any \mathbf{a}_L satisfying $(\mathbf{a}_L)_{y^*} = \max_i (\mathbf{a}_L)_i$, formula 23 holds.

$$\|\mathbf{a}_L - \hat{\mathbf{a}}_L\|_{L_1} \geq \max_i (\hat{\mathbf{a}}_L)_i - (\hat{\mathbf{a}}_L)_{y^*} = \|\mathbf{a}_L^{MA} - \hat{\mathbf{a}}_L\|_{L_1} \quad (23)$$

This completes the proof. ■

(b). When $\|\cdot\|_N$ is set to the L2 norm, we introduce Lagrangian multipliers $\mu \in \mathbb{R}^{n_L-1}$ for constraints in problem 21. For any $\mu_i = 0$, the corresponding constraint is not active, i.e., $(\mathbf{a}_L)_{y^*} > (\mathbf{a}_L)_i$, while when $\mu_i > 0$, the corresponding constraint is active, i.e., $(\mathbf{a}_L)_{y^*} = (\mathbf{a}_L)_i$. The Lagrangian function is as follows.

$$L(\mathbf{a}_L, \mu) = \mathbf{a}_L^T \mathbf{a}_L - 2\mathbf{a}_L^T \hat{\mathbf{a}}_L + \hat{\mathbf{a}}_L^T \hat{\mathbf{a}}_L - \sum_{i \in I_{y^*}} \mu_i [(\mathbf{a}_L)_{y^*} - (\mathbf{a}_L)_i] \quad (24)$$

Since problem 21 is a convex quadratic problem satisfying Slater's condition [5], it has a unique solution \mathbf{a}_L^* . Hence, there exists a unique solution (\mathbf{a}_L^*, μ^*) for the KKT conditions 25.

$$\begin{cases} (\mathbf{a}_L^*)_{y^*} \geq \max_i (\mathbf{a}_L^*)_i & (25a) \end{cases}$$

$$\begin{cases} \mu^* \succeq 0 & (25b) \end{cases}$$

$$\begin{cases} \frac{\partial L}{\partial (\mathbf{a}_L^*)_{y^*}} (\mathbf{a}_L^*, \mu^*) = 2(\mathbf{a}_L^* - \hat{\mathbf{a}}_L)_{y^*} - \sum_{i \in I_{y^*}} \mu_i^* = 0 & (25c) \end{cases}$$

$$\begin{cases} \frac{\partial L}{\partial (\mathbf{a}_L^*)_i} (\mathbf{a}_L^*, \mu^*) = 2(\mathbf{a}_L^* - \hat{\mathbf{a}}_L)_i + \mu_i^* = 0 & (25d) \end{cases}$$

$$\begin{cases} \mu_i^* [(\mathbf{a}_L^*)_{y^*} - (\mathbf{a}_L^*)_i] = 0, \forall i \in I_{y^*} & (25e) \end{cases}$$

According to condition 25 c and d, we can eliminate \mathbf{a}_L^* by

$$(\mathbf{a}_L^*)_{y^*} = (\hat{\mathbf{a}}_L)_{y^*} + \frac{\sum_{i \in I_{y^*}} \mu_i^*}{2} \quad (26)$$

$$(\mathbf{a}_L^*)_i = (\hat{\mathbf{a}}_L)_i - \frac{\mu_i^*}{2}, \forall i \in I_{y^*} \quad (27)$$

It is clear that $(\mathbf{a}_L^*)_{y^*} \geq (\hat{\mathbf{a}}_L)_{y^*}$ and $(\mathbf{a}_L^*)_i \leq (\hat{\mathbf{a}}_L)_i, \forall i \in I_{y^*}$. The KKT condition 25 suffices to solve all μ_i^* , which we split into three cases:

(i) For all $i \in I_1 = \{i | (\hat{\mathbf{a}}_L)_{y^*} \geq (\hat{\mathbf{a}}_L)_i\}$, the i^{th} entry of vector $(\mathbf{a}_L^*)_i$ can contribute zero to the L2 norm difference by letting $\mu_i^* = 0$ and $(\mathbf{a}_L^*)_i = (\hat{\mathbf{a}}_L)_i$.

(ii) For all $i \in I_2 = \{i | (\hat{\mathbf{a}}_L)_{y^*} < (\hat{\mathbf{a}}_L)_i, (\mathbf{a}_L^*)_{y^*} > (\mathbf{a}_L^*)_i\}$, we get inequation 28 by Eq. 26, Eq. 27 and $\mu_i^* = 0$ by condition 25 e.

$$\frac{\sum_{k \in I_{y^*}} \mu_k^*}{2} > (\mathbf{a}_L^*)_i - (\hat{\mathbf{a}}_L)_{y^*} = (\hat{\mathbf{a}}_L)_i - (\hat{\mathbf{a}}_L)_{y^*} \quad (28)$$

(iii) The "active set" $I_3 = \{i | (\hat{\mathbf{a}}_L)_{y^*} < (\hat{\mathbf{a}}_L)_i, (\mathbf{a}_L^*)_{y^*} = (\mathbf{a}_L^*)_i\}$ suggests $\mu_{I_3}^* \succ 0$ and the corresponding constraints are active. For all $i \in I_3$ we have Eq. 29 by Eq. 26 and 27.

$$\frac{\sum_k \mu_k^*}{2} + \frac{\mu_i^*}{2} = (\hat{\mathbf{a}}_L)_i - (\hat{\mathbf{a}}_L)_{y^*} \quad (29)$$

That is, $(\mathbf{1}_{|I_3|} + \mathbb{I}_{|I_3|}) \frac{\mu_{I_3}^*}{2} = ((\hat{\mathbf{a}}_L)_i - (\hat{\mathbf{a}}_L)_{y^*})_{I_3}$. Through matrix inversion, equation 30 will hold, where $\mathbb{I}_{|I_3|}$ indicates the $|I_3|$ -dimensional identity matrix, and $\mathbf{1}_{|I_3|}$ indicates the $|I_3|$ -dimensional matrix with all entries equal to 1.

$$\frac{\mu_{I_3}^*}{2} = (\mathbb{I}_{|I_3|} - \frac{\mathbf{1}_{|I_3|}}{|I_3| + 1})((\hat{\mathbf{a}}_L)_i - (\hat{\mathbf{a}}_L)_{y^*})_{I_3} \quad (30)$$

Therefore, as long as the sets I_1 , I_2 and I_3 are determined, we can obtain μ^* and thus \mathbf{a}_L^* . The index set I_1 is straightforward

to identify, whereas I_2 and I_3 must be considered jointly. By summing Eq. 29 over all $i \in I_3$, we obtain Eq. 31.

$$\frac{\sum_{k \in I_{y^*}} \mu_k^*}{2} = \frac{\sum_{k \in I_3} [(\hat{\mathbf{a}}_L)_k - (\hat{\mathbf{a}}_L)_{y^*}]}{|I_3| + 1} \quad (31)$$

Hence, for all $j \in I_2, i \in I_3$, we have inequation 32 by formula 28, 29, and 31.

$$(\hat{\mathbf{a}}_L)_j - (\hat{\mathbf{a}}_L)_{y^*} < \frac{\sum_{k \in I_3} [(\hat{\mathbf{a}}_L)_k - (\hat{\mathbf{a}}_L)_{y^*}]}{|I_3| + 1} < (\hat{\mathbf{a}}_L)_i - (\hat{\mathbf{a}}_L)_{y^*} \quad (32)$$

Let $\{d_s = (\hat{\mathbf{a}}_L)_{t_s} - (\hat{\mathbf{a}}_L)_{y^*}\}_{t_s \in I_2 \cup I_3}$ be a monotonically decreasing sequence. It is easy to get $(\hat{\mathbf{a}}_L)_j < (\hat{\mathbf{a}}_L)_i, \forall j \in I_2, i \in I_3$. Thus, we can determine set I_2 and I_3 in $\{d_s\}$ by rewriting equation 32 as follows.

$$(|I_3| + 1)d_{|I_3|+1} < \sum_{s=1}^{|I_3|} d_s < (|I_3| + 1)d_{|I_3|} \quad (33)$$

Due to the existence and uniqueness of the Lagrange multipliers μ^* , there must exist a unique number of $|I_3|$, which can be achieved by checking all indices $\{1, 2, \dots, |I_2| + |I_3|\}$ against formula 33. Then, we have $I_3 = \{t_s\}_{s=1}^{|I_3|}$. We call the obtained \mathbf{a}_L^* "nearest embedding" solution \mathbf{a}_L^{NE} .

Algorithm 1 Parallelizable Nearest Embedding Algorithm

Require: original output vector $\hat{\mathbf{a}}_L$ and ground truth label y^*

Ensure: reconstructed output vector \mathbf{a}_L^{NE}

- 1: $\mathbf{a}_L^{NE} \leftarrow \hat{\mathbf{a}}_L$
 - 2: Get the difference sequence $\{d_i\}_{i=1}^{n_L}$, where $d_i \leftarrow (\hat{\mathbf{a}}_L)_i - (\hat{\mathbf{a}}_L)_{y^*}$.
 - 3: Sort $\{d_i\}_{i=1}^{n_L}$ to get the monotonically decreasing sequence $\{d_s\}_{s=1}^{n_L}$, where $d_s \leftarrow (\hat{\mathbf{a}}_L)_{t_s} - (\hat{\mathbf{a}}_L)_{y^*}$.
 - 4: Get the cumulate sum $\{c_w\}$, where $c_w \leftarrow \sum_{s=1}^w d_s$.
 - 5: Get sequences $\{s \cdot d_s\}$ and $\{(s+1) \cdot d_s\}$.
 - 6: Find the unique index $s = |I_3|$ that satisfies $d_{|I_3|} > 0$ and formula 33.
 - 7: Get index set $I_3 \leftarrow \{t_s\}_{s=1}^{|I_3|}$ and calculate $\mu_{I_3}^*$ by equation 30. Set other $\mu_i^* \leftarrow 0$.
 - 8: Update \mathbf{a}_L^{NE} by equations 26 and 27.
 - 9: **return** \mathbf{a}_L^{NE}
-

3.4 Other Reverse Operations

We next discuss the reverse computation of other operations classically occurred in CNNs.

(a) **Non-linear Activation.** Common activation functions mapping \mathbf{z}_l to \mathbf{a}_l can be divided into three types:

(i) Bijection with unlimited range (e.g. leaky relu, sinh, arcsinh). Their inverse functions has domain of \mathbb{R} , naturally suitable for the reverse computation sending \mathbf{a}_l^* to \mathbf{z}_l^* .

(ii) Bijection with limited range (e.g. sigmoid, arctan). \mathbf{a}_l^* may not within the domain of these activations' inverse functions. Hence, we firstly limit \mathbf{a}_l^* to fit the domain of their inverse functions, and then perform the reverse computation.

Table 1: modules post-training results of a baseline on Mnist with test accuracy 97.62% (loss coefficient $\alpha = 0.1$)

PT (l_S, l_R)	#paras	GPU Mem	epoch1	epoch5	epoch10
BP(0,1)	52	7.93	97.693 \pm 0.035	97.671 \pm 0.062	97.719\pm0.054
FR(0,1)	52	8.23	97.682 \pm 0.042	97.688 \pm 0.037	97.692 \pm 0.039
BP(0,2)	256	7.93	97.703 \pm 0.031	97.707 \pm 0.038	97.748\pm0.023
FR(0,2)	256	8.20	97.682 \pm 0.040	97.707 \pm 0.026	97.739 \pm 0.021
BP(1,2)	204	5.37	97.700 \pm 0.022	97.712 \pm 0.018	97.694 \pm 0.022
FR(1,2)	204	5.64	97.695 \pm 0.020	97.697 \pm 0.018	97.716\pm0.028
BP(0,3)	2826	7.96	97.736 \pm 0.030	97.855 \pm 0.054	97.913\pm0.062
FR(0,3)	2826	7.98	97.676 \pm 0.036	97.744 \pm 0.047	97.781 \pm 0.058
BP(1,3)	2774	5.40	97.727 \pm 0.065	97.833 \pm 0.072	97.901\pm0.047
FR(1,3)	2774	5.41	97.695 \pm 0.045	97.748 \pm 0.057	97.791 \pm 0.031
BP(2,3)	2570	5.39	97.718 \pm 0.046	97.826 \pm 0.023	97.852\pm0.036
FR(2,3)	2570	5.41	97.692 \pm 0.047	97.742 \pm 0.023	97.741 \pm 0.034

Table 2: modules post-training results of a baseline on Cifar10 with test accuracy 62.55% (loss coefficient $\alpha = 0.1$)

PT (l_S, l_R)	#paras	GPU Mem	epoch1	epoch5	epoch10
BP(0,1)	380	17.43	62.474 \pm 0.173	62.568 \pm 0.256	62.667 \pm 0.244
FR(0,1)	380	20.45	62.336 \pm 0.326	62.584 \pm 0.472	62.722\pm0.288
BP(0,2)	840	17.43	62.546 \pm 0.202	62.569 \pm 0.321	62.736\pm0.226
FR(0,2)	840	19.60	62.371 \pm 0.323	62.420 \pm 0.183	62.600 \pm 0.241
BP(1,2)	460	12.01	62.698\pm0.155	62.674 \pm 0.109	62.622 \pm 0.084
FR(1,2)	460	13.94	62.667 \pm 0.085	62.684 \pm 0.095	62.603 \pm 0.122
BP(0,3)	2205	17.45	62.294 \pm 0.399	62.717 \pm 0.253	62.749 \pm 0.177
FR(0,3)	2205	19.46	62.465 \pm 0.254	62.637 \pm 0.283	62.755\pm0.386
BP(1,3)	1825	12.03	62.662 \pm 0.125	62.719 \pm 0.141	62.775\pm0.203
FR(1,3)	1825	13.79	62.576 \pm 0.102	62.696 \pm 0.143	62.653 \pm 0.103
BP(2,3)	1365	12.02	62.564 \pm 0.146	62.593\pm0.183	62.498 \pm 0.114
FR(2,3)	1365	13.08	62.505 \pm 0.102	62.543 \pm 0.145	62.575 \pm 0.161
BP(0,4)	33053	17.81	62.415 \pm 0.375	62.654 \pm 0.433	62.711 \pm 0.549
FR(0,4)	33053	19.65	62.393 \pm 0.313	62.693 \pm 0.194	62.982\pm0.215
BP(1,4)	32673	12.38	62.451 \pm 0.265	62.700 \pm 0.184	62.682 \pm 0.177
FR(1,4)	32673	13.99	62.481 \pm 0.148	62.856 \pm 0.242	62.883\pm0.120
BP(2,4)	32213	12.37	62.383 \pm 0.236	62.639 \pm 0.220	62.533 \pm 0.199
FR(2,4)	32213	13.28	62.544 \pm 0.185	62.656\pm0.143	62.587 \pm 0.109
BP(3,4)	30848	12.35	62.526 \pm 0.256	62.691 \pm 0.084	62.715\pm0.122
FR(3,4)	30848	13.26	62.535 \pm 0.143	62.703 \pm 0.091	62.692 \pm 0.145
BP(0,5)	34343	17.95	62.137 \pm 0.244	62.588 \pm 0.442	62.583 \pm 0.319
FR(0,5)	34343	19.51	62.239 \pm 0.305	62.631 \pm 0.230	62.878\pm0.198
BP(1,5)	33963	12.40	62.369 \pm 0.290	62.807\pm0.305	62.582 \pm 0.112
FR(1,5)	33963	13.84	62.340 \pm 0.239	62.695 \pm 0.143	62.719 \pm 0.200
BP(2,5)	33503	12.39	62.360 \pm 0.215	62.612\pm0.174	62.445 \pm 0.190
FR(2,5)	33503	13.13	62.384 \pm 0.197	62.586 \pm 0.242	62.544 \pm 0.163
BP(3,5)	32138	12.37	62.383 \pm 0.109	62.579\pm0.116	62.447 \pm 0.149
FR(3,5)	32138	13.11	62.348 \pm 0.188	62.568 \pm 0.239	62.522 \pm 0.170
BP(4,5)	1290	12.02	62.301 \pm 0.152	62.365\pm0.111	62.260 \pm 0.071
FR(4,5)	1290	12.76	62.263 \pm 0.104	62.309 \pm 0.154	62.272 \pm 0.053

(iii) Not bijection with limited range (e.g. relu, sin). We choose identity map as relu’s reverse compute. As for locally bijective functions like sin, a_i^* is normalized into $[-1, 1]$ and then deactivated by their inverse functions.

Table 3: modules post-training results of a baseline on Cifar100 with test accuracy 36.74% (loss coefficient $\alpha = 0.7$)

PT (l_S, l_R)	#paras	GPU Mem	epoch1	epoch5	epoch10
BP(0,1)	760	26.51	36.806 \pm 0.269	36.901 \pm 0.214	36.972\pm0.199
FR(0,1)	760	34.18	36.957 \pm 0.224	36.661 \pm 0.386	36.904 \pm 0.250
BP(0,2)	2125	26.53	36.846 \pm 0.265	36.858\pm0.172	36.780 \pm 0.216
FR(0,2)	2125	30.95	36.695 \pm 0.345	36.785 \pm 0.237	36.515 \pm 0.449
BP(1,2)	1365	19.83	37.158\pm0.127	37.090 \pm 0.089	37.072 \pm 0.136
FR(1,2)	1365	22.70	37.005 \pm 0.158	36.990 \pm 0.094	37.058 \pm 0.083
BP(0,3)	4845	26.56	36.594 \pm 0.272	36.455 \pm 0.183	36.329 \pm 0.300
FR(0,3)	4845	30.66	36.814 \pm 0.229	36.930 \pm 0.259	37.045\pm0.324
BP(1,3)	4085	19.87	36.905 \pm 0.138	36.771 \pm 0.122	36.626 \pm 0.160
FR(1,3)	4085	22.40	37.042 \pm 0.206	37.120 \pm 0.245	37.198\pm0.118
BP(2,3)	2720	19.85	37.082 \pm 0.117	36.932 \pm 0.077	36.734 \pm 0.068
FR(2,3)	2720	22.38	37.108 \pm 0.148	37.197\pm0.112	37.100 \pm 0.089
BP(0,4)	87021	27.50	36.366 \pm 0.255	36.243 \pm 0.394	35.941 \pm 0.193
FR(0,4)	87021	31.51	36.759\pm0.178	36.543 \pm 0.267	36.464 \pm 0.249
BP(1,4)	86261	20.81	36.809 \pm 0.196	36.659 \pm 0.122	36.319 \pm 0.160
FR(1,4)	86261	23.25	36.866\pm0.216	36.839 \pm 0.168	36.666 \pm 0.107
BP(2,4)	84896	20.79	36.932\pm0.136	36.706 \pm 0.171	36.429 \pm 0.133
FR(2,4)	84896	23.23	36.895 \pm 0.140	36.816 \pm 0.137	36.725 \pm 0.109
BP(3,4)	82176	20.76	37.063 \pm 0.113	37.029 \pm 0.178	36.923 \pm 0.149
FR(3,4)	82176	23.19	37.191\pm0.100	37.081 \pm 0.159	37.084 \pm 0.173
BP(0,5)	112721	27.80	36.109 \pm 0.289	35.852 \pm 0.324	35.531 \pm 0.578
FR(0,5)	112721	31.56	36.865 \pm 0.117	37.007 \pm 0.332	37.179\pm0.138
BP(1,5)	111961	21.10	36.426 \pm 0.249	36.427 \pm 0.273	35.561 \pm 0.202
FR(1,5)	111961	23.29	36.957 \pm 0.092	37.116 \pm 0.113	37.215\pm0.155
BP(2,5)	110596	21.08	36.562 \pm 0.223	36.606 \pm 0.206	35.758 \pm 0.141
FR(2,5)	110596	23.28	36.962 \pm 0.231	37.007 \pm 0.150	37.038\pm0.157
BP(3,5)	107876	21.05	36.801 \pm 0.239	36.738 \pm 0.183	36.463 \pm 0.112
FR(3,5)	107876	23.24	37.040 \pm 0.076	37.042 \pm 0.106	37.108\pm0.099
BP(4,5)	25700	20.11	36.999 \pm 0.088	37.069 \pm 0.143	36.995 \pm 0.128
FR(4,5)	25700	22.30	37.050 \pm 0.112	37.087\pm0.086	37.065 \pm 0.069

(b) **Pooling Layers (stride=kernel size).** Since the information lost during pooling operations contributes little to the final output, we reconstruct the pre-pooling feature maps by directly copying values from the post-pooling ones.

4 Experiments

To evaluate FR-based post-training (FR-PT), experiments on six classical image classification benchmarks are conducted. We choose a 2Conv+1fc architecture as the baseline network for Mnist, a 3Conv+2fc for Cifar-10, a 3Conv+2fc for Cifar-100, a 4Conv+2fc for Tiny ImageNet, a 5Conv+2fc for ImageNet, and a 5Conv+2fc for ImageWoof.

Data sets are all instance normalized as the default setting following the previous works [29]. All nonlinear activation functions are "tanh". The pooling layers are configured as max-pooling, with their stride equal to the kernel size. The optimizer for BP is Adam with a learning rate 0.001. The batch size is set to 256 for all training processes. The performance of each network is evaluated by its test accuracy (%).

Table 4: modules post-training results of a baseline on Tiny ImageNet with test accuracy 24.99% (loss coefficient $\alpha = 0.7$)

PT (l_S, l_R)	#paras	GPU Mem	epoch1	epoch5	epoch10
BP(0,1)	760	137.26	24.945 \pm 0.186	25.187\pm0.159	25.100 \pm 0.206
FR(0,1)	760	171.37	24.533 \pm 0.232	24.724 \pm 0.165	24.829 \pm 0.160
BP(0,2)	3035	139.30	25.408 \pm 0.486	25.412\pm0.518	25.413 \pm 0.291
FR(0,2)	3035	157.21	25.373 \pm 0.336	25.368 \pm 0.254	25.375 \pm 0.445
BP(1,2)	2275	109.77	25.116 \pm 0.383	25.511 \pm 0.342	25.427 \pm 0.306
FR(1,2)	2275	136.53	25.365 \pm 0.533	25.697\pm0.442	25.339 \pm 0.464
BP(0,3)	10945	139.79	25.264 \pm 0.447	25.455\pm0.368	25.430 \pm 0.452
FR(0,3)	10945	150.54	25.216 \pm 0.344	25.144 \pm 0.702	25.199 \pm 0.439
BP(1,3)	10185	109.46	25.013 \pm 0.391	25.523 \pm 0.313	25.270 \pm 0.457
FR(1,3)	10185	129.06	25.618\pm0.350	25.098 \pm 0.694	25.587 \pm 0.480
BP(2,3)	7910	106.57	25.702\pm0.314	25.663 \pm 0.337	25.647 \pm 0.287
FR(2,3)	7910	119.06	25.624 \pm 0.170	25.521 \pm 0.286	25.502 \pm 0.306
BP(0,4)	25165	140.19	25.072 \pm 0.597	25.092 \pm 0.642	24.805 \pm 0.363
FR(0,4)	25165	150.09	25.189 \pm 0.734	25.334 \pm 0.544	25.713\pm0.498
BP(1,4)	24405	109.63	25.072 \pm 0.554	24.942 \pm 0.547	24.531 \pm 0.363
FR(1,4)	24405	127.44	25.439 \pm 0.474	25.303 \pm 0.634	25.523\pm0.378
BP(2,4)	22130	106.73	25.372 \pm 0.447	25.078 \pm 0.481	25.005 \pm 0.371
FR(2,4)	22130	117.78	25.533 \pm 0.614	25.698\pm0.416	25.377 \pm 0.303
BP(3,4)	14220	106.64	25.696 \pm 0.341	25.462 \pm 0.213	25.442 \pm 0.225
FR(3,4)	14220	116.77	25.601 \pm 0.298	25.717 \pm 0.242	25.945\pm0.299
BP(0,5)	394317	143.84	25.341 \pm 0.534	25.151 \pm 0.418	24.288 \pm 0.263
FR(0,5)	394317	153.10	26.408\pm0.349	26.117 \pm 0.698	25.474 \pm 0.358
BP(1,5)	393557	113.96	25.528 \pm 0.427	24.694 \pm 0.483	23.529 \pm 0.369
FR(1,5)	393557	130.46	25.861 \pm 0.313	25.979\pm0.342	25.403 \pm 0.282
BP(2,5)	391282	111.49	25.547 \pm 0.328	25.001 \pm 0.443	23.829 \pm 0.292
FR(2,5)	391282	121.79	26.346\pm0.250	25.883 \pm 0.342	25.380 \pm 0.285
BP(3,5)	383372	112.46	26.031 \pm 0.371	25.454 \pm 0.233	24.526 \pm 0.244
FR(3,5)	383372	121.69	26.410\pm0.261	26.097 \pm 0.191	25.434 \pm 0.321
BP(4,5)	369152	111.87	26.779\pm0.194	26.173 \pm 0.159	25.539 \pm 0.195
FR(4,5)	369152	121.77	26.421 \pm 0.140	26.391 \pm 0.144	26.068 \pm 0.176
BP(0,6)	496917	144.96	24.824 \pm 0.606	23.969 \pm 0.338	21.866 \pm 0.213
FR(0,6)	496917	153.55	25.885 \pm 0.222	26.359\pm0.149	26.104 \pm 0.401
BP(1,6)	496157	114.50	24.592 \pm 0.472	23.707 \pm 0.461	21.342 \pm 0.376
FR(1,6)	496157	131.68	26.008\pm0.284	25.934 \pm 0.365	25.968 \pm 0.155
BP(2,6)	493882	114.05	24.780 \pm 0.568	23.588 \pm 0.295	21.456 \pm 0.298
FR(2,6)	493882	122.63	25.883 \pm 0.223	26.116\pm0.208	26.055 \pm 0.213
BP(3,6)	485972	112.99	25.504 \pm 0.267	24.258 \pm 0.267	21.780 \pm 0.237
FR(3,6)	485972	122.54	25.925 \pm 0.206	26.008\pm0.151	25.846 \pm 0.204
BP(4,6)	471752	112.28	25.826 \pm 0.257	24.655 \pm 0.337	22.908 \pm 0.187
FR(4,6)	471752	122.37	26.079\pm0.166	26.061 \pm 0.228	26.014 \pm 0.128
BP(5,6)	102600	108.57	25.630 \pm 0.186	25.148 \pm 0.221	24.283 \pm 0.252
FR(5,6)	102600	117.48	25.686 \pm 0.144	25.807\pm0.214	25.794 \pm 0.151

Section 4.1 compares FR-based post-training (FR-PT) with the SOTA BP-based post-training (BP-PT) across six benchmarks, and visualizes the deviations between the forward and reconstructed feature maps. Section 4.2 demonstrates ablation experiments to verify the necessary of optimal embedding methods. Section 4.3 studies the effect of FR-PT on networks at different training stages. Lastly, we discuss the effectiveness of FR-PT on different network architectures in Section 4.4.

4.1 Post-Training Results

We first define and train a baseline CNN architecture for each dataset, in which the number of channels in convolutional layers typically increases with depth, while the dimensionality

Table 5: modules post training results of a baseline on ImageNet with test accuracy 51.56% (loss coefficient $\alpha = 0.3$)

PT (l_S, l_R)	#paras	GPU Mem	epoch1	epoch5	epoch10
BP(0,1)	18760	1320.80	50.652 \pm 0.455	51.399 \pm 0.419	51.554 \pm 0.435
FR(0,1)	18760	1600.61	50.978 \pm 0.595	51.490 \pm 0.755	51.651\pm0.589
BP(0,2)	62125	1321.29	50.983 \pm 0.512	51.427 \pm 0.446	51.850 \pm 0.306
FR(0,2)	62125	1491.10	51.238 \pm 0.236	51.608 \pm 0.365	51.939\pm0.488
BP(1,2)	43365	1074.74	51.544 \pm 0.169	51.806 \pm 0.301	51.954 \pm 0.200
FR(1,2)	43365	1239.19	51.503 \pm 0.201	51.704 \pm 0.207	52.010\pm0.300
BP(0,3)	98445	1369.04	50.601 \pm 0.553	51.429 \pm 0.671	51.911 \pm 0.599
FR(0,3)	98445	1460.55	50.678 \pm 0.564	51.511 \pm 0.364	52.217\pm0.432
BP(1,3)	79685	1075.16	51.282 \pm 0.351	52.048 \pm 0.466	52.194 \pm 0.346
FR(1,3)	79685	1211.42	51.567 \pm 0.404	51.939 \pm 0.339	52.336\pm0.165
BP(2,3)	36320	1074.66	51.470 \pm 0.205	51.669 \pm 0.368	51.521 \pm 0.368
FR(2,3)	36320	1211.07	51.671 \pm 0.102	51.814\pm0.270	51.794 \pm 0.243
BP(0,4)	110970	1369.18	50.150 \pm 0.560	51.024 \pm 0.756	52.183\pm0.532
FR(0,4)	110970	1454.04	50.668 \pm 0.660	51.791 \pm 0.329	52.150 \pm 0.418
BP(1,4)	92210	1075.31	51.478 \pm 0.653	51.903 \pm 0.495	52.201\pm0.440
FR(1,4)	92210	1205.89	51.289 \pm 0.397	51.936 \pm 0.262	52.061 \pm 0.380
BP(2,4)	48845	1074.81	51.208 \pm 0.239	51.712 \pm 0.432	52.064\pm0.259
FR(2,4)	48845	1204.80	51.697 \pm 0.356	51.569 \pm 0.318	51.916 \pm 0.318
BP(3,4)	12525	1074.39	51.439 \pm 0.340	51.712\pm0.255	51.496 \pm 0.238
FR(3,4)	12525	1204.40	51.468 \pm 0.322	51.575 \pm 0.304	51.534 \pm 0.251
BP(0,5)	117750	1369.26	49.934 \pm 0.872	51.557 \pm 0.657	52.275\pm0.491
FR(0,5)	117750	1453.52	50.288 \pm 0.588	51.651 \pm 0.529	52.005 \pm 0.580
BP(1,5)	98990	1075.39	51.378 \pm 0.527	51.908 \pm 0.267	52.301\pm0.289
FR(1,5)	98990	1205.44	51.409 \pm 0.433	52.270 \pm 0.342	52.265 \pm 0.421
BP(2,5)	55625	1074.89	51.205 \pm 0.552	51.814 \pm 0.299	52.176\pm0.336
FR(2,5)	55625	1204.33	51.315 \pm 0.391	51.707 \pm 0.138	52.000 \pm 0.513
BP(3,5)	19305	1074.47	51.722 \pm 0.343	51.575 \pm 0.291	51.676 \pm 0.372
FR(3,5)	19305	1203.91	51.404 \pm 0.419	51.674 \pm 0.402	51.789\pm0.280
BP(4,5)	6780	1074.32	51.600 \pm 0.237	51.901 \pm 0.110	52.120\pm0.188
FR(4,5)	6780	1203.78	51.717 \pm 0.197	52.082 \pm 0.215	52.076 \pm 0.118
BP(0,6)	179318	1369.97	49.343 \pm 0.749	50.874 \pm 0.684	51.233 \pm 0.971
FR(0,6)	179318	1453.65	50.107 \pm 0.817	50.803 \pm 0.497	51.462\pm0.420
BP(1,6)	160558	1076.09	50.668 \pm 0.518	51.496 \pm 0.442	51.073 \pm 0.316
FR(1,6)	160558	1205.68	51.139 \pm 0.390	51.687\pm0.656	51.287 \pm 0.495
BP(2,6)	117193	1075.59	50.563 \pm 0.610	51.121 \pm 0.600	50.780 \pm 0.392
FR(2,6)	117193	1204.57	51.083 \pm 0.579	51.439\pm0.469	50.996 \pm 0.309
BP(3,6)	80873	1075.17	51.011 \pm 0.470	51.050 \pm 0.315	51.124 \pm 0.347
FR(3,6)	80873	1204.16	51.389\pm0.424	51.200 \pm 0.342	51.172 \pm 0.278
BP(4,6)	68348	1075.03	51.447 \pm 0.420	51.447 \pm 0.250	51.434 \pm 0.362
FR(4,6)	68348	1204.01	51.350 \pm 0.433	51.712\pm0.333	51.468 \pm 0.327
BP(5,6)	61568	1074.95	51.654 \pm 0.217	51.755 \pm 0.267	51.592 \pm 0.369
FR(5,6)	61568	1203.93	51.524 \pm 0.301	51.664\pm0.162	51.501 \pm 0.222
BP(0,7)	180608	1369.98	49.855 \pm 0.542	51.294 \pm 0.351	51.009 \pm 0.483
FR(0,7)	180608	1453.49	50.586 \pm 0.627	51.361\pm0.602	51.129 \pm 0.202
BP(1,7)	161848	1076.11	50.665 \pm 0.522	51.159 \pm 0.600	50.280 \pm 0.336
FR(1,7)	161848	1205.54	51.101 \pm 0.422	51.366\pm0.225	51.034 \pm 0.202
BP(2,7)	118483	1075.61	50.818 \pm 0.359	50.932 \pm 0.369	49.804 \pm 0.386
FR(2,7)	118483	1204.43	51.106 \pm 0.475	51.129\pm0.354	50.736 \pm 0.430
BP(3,7)	82163	1075.19	51.118 \pm 0.381	51.004 \pm 0.541	50.466 \pm 0.363
FR(3,7)	82163	1204.02	51.177 \pm 0.271	51.190\pm0.344	51.106 \pm 0.312
BP(4,7)	69638	1075.05	51.274 \pm 0.232	51.075 \pm 0.286	50.782 \pm 0.317
FR(4,7)	69638	1203.87	51.292 \pm 0.226	51.307\pm0.197	51.238 \pm 0.289
BP(5,7)	62858	1074.97	51.264 \pm 0.272	51.350 \pm 0.380	50.889 \pm 0.220
FR(5,7)	62858	1203.79	51.389 \pm 0.269	51.468\pm0.253	51.394 \pm 0.218
BP(6,7)	1290	1074.26	51.501\pm0.190	51.468 \pm 0.112	51.192 \pm 0.136
FR(6,7)	1290	1203.09	51.409 \pm 0.070	51.340 \pm 0.135	51.126 \pm 0.096

Table 6: modules post training results of a baseline on ImageWoof with test accuracy 27.23% (loss coefficient $\alpha = 0.1$)

PT (l_S, l_R)	#paras	GPU Mem	epoch1	epoch5	epoch10
BP(0,1)	18760	1320.80	27.255 ± 0.249	27.210 ± 0.178	27.156 ± 0.210
FR(0,1)	18760	1606.72	27.199 ± 0.279	27.247 ± 0.236	27.180 ± 0.170
BP(0,2)	62125	1321.29	27.320 ± 0.320	27.391 ± 0.329	27.381 ± 0.247
FR(0,2)	62125	1491.90	27.109 ± 0.205	27.246 ± 0.245	27.368 ± 0.337
BP(1,2)	43365	966.78	27.241 ± 0.192	27.170 ± 0.145	27.350 ± 0.253
FR(1,2)	43365	1101.77	27.223 ± 0.307	27.185 ± 0.197	27.353 ± 0.219
BP(0,3)	98445	1369.04	27.218 ± 0.269	27.414 ± 0.267	27.274 ± 0.359
FR(0,3)	98445	1461.20	27.162 ± 0.241	27.287 ± 0.189	27.160 ± 0.296
BP(1,3)	79685	967.20	27.413 ± 0.318	27.286 ± 0.321	27.354 ± 0.224
FR(1,3)	79685	1069.39	27.394 ± 0.335	27.311 ± 0.344	27.289 ± 0.272
BP(2,3)	36320	966.70	27.460 ± 0.315	27.490 ± 0.182	27.437 ± 0.262
FR(2,3)	36320	1069.00	27.455 ± 0.270	27.462 ± 0.264	27.554 ± 0.302
BP(0,4)	110970	1369.18	27.289 ± 0.332	27.371 ± 0.343	27.386 ± 0.443
FR(0,4)	110970	1453.97	27.185 ± 0.197	27.228 ± 0.384	27.111 ± 0.256
BP(1,4)	92210	967.35	27.424 ± 0.356	27.261 ± 0.403	27.279 ± 0.311
FR(1,4)	92210	1062.41	27.666 ± 0.336	27.447 ± 0.326	27.231 ± 0.369
BP(2,4)	48845	966.85	27.343 ± 0.230	27.381 ± 0.181	27.149 ± 0.303
FR(2,4)	48845	1061.90	27.526 ± 0.253	27.381 ± 0.283	27.198 ± 0.344
BP(3,4)	12525	966.43	27.432 ± 0.273	27.608 ± 0.243	27.539 ± 0.284
FR(3,4)	12525	1061.50	27.587 ± 0.280	27.559 ± 0.186	27.470 ± 0.448
BP(0,5)	117750	1369.26	27.137 ± 0.387	26.778 ± 0.367	26.709 ± 0.357
FR(0,5)	117750	1453.45	27.088 ± 0.350	27.190 ± 0.272	26.900 ± 0.402
BP(1,5)	98990	967.42	27.231 ± 0.242	27.302 ± 0.359	26.679 ± 0.331
FR(1,5)	98990	1061.86	27.478 ± 0.296	27.167 ± 0.481	26.554 ± 0.426
BP(2,5)	55625	966.93	27.244 ± 0.427	27.098 ± 0.395	26.801 ± 0.461
FR(2,5)	55625	1061.36	27.577 ± 0.612	27.185 ± 0.430	26.539 ± 0.293
BP(3,5)	19305	966.51	27.378 ± 0.238	27.294 ± 0.304	27.193 ± 0.325
FR(3,5)	19305	1060.96	27.630 ± 0.272	27.585 ± 0.339	27.037 ± 0.231
BP(4,5)	6780	966.36	27.849 ± 0.248	27.468 ± 0.254	27.292 ± 0.312
FR(4,5)	6780	1060.81	27.903 ± 0.353	27.544 ± 0.120	27.333 ± 0.215
BP(0,6)	179318	1369.97	26.895 ± 0.589	26.419 ± 0.593	25.963 ± 0.555
FR(0,6)	179318	1453.64	26.946 ± 0.489	26.681 ± 0.472	25.513 ± 0.578
BP(1,6)	160558	968.13	27.109 ± 0.381	26.472 ± 0.350	25.772 ± 0.512
FR(1,6)	160558	1062.06	26.918 ± 0.766	26.589 ± 0.430	25.826 ± 0.524
BP(2,6)	117193	967.63	27.205 ± 0.506	26.276 ± 0.452	25.551 ± 0.299
FR(2,6)	117193	1061.56	27.322 ± 0.354	26.416 ± 0.509	25.976 ± 0.297
BP(3,6)	80873	967.21	27.338 ± 0.346	26.821 ± 0.517	25.991 ± 0.507
FR(3,6)	80873	1061.15	27.310 ± 0.268	26.679 ± 0.577	26.259 ± 0.235
BP(4,6)	68348	967.07	27.442 ± 0.381	27.060 ± 0.347	26.859 ± 0.491
FR(4,6)	68348	1061.00	27.714 ± 0.349	27.256 ± 0.397	27.004 ± 0.416
BP(5,6)	61568	966.99	27.745 ± 0.227	27.633 ± 0.250	27.126 ± 0.215
FR(5,6)	61568	1060.92	27.821 ± 0.326	27.587 ± 0.351	27.129 ± 0.215
BP(0,7)	180608	1369.98	27.394 ± 0.527	26.187 ± 0.419	25.220 ± 0.646
FR(0,7)	180608	1453.49	26.933 ± 0.645	26.292 ± 0.483	25.429 ± 0.517
BP(1,7)	161848	968.15	27.043 ± 0.383	26.215 ± 0.340	25.345 ± 0.551
FR(1,7)	161848	1061.91	27.088 ± 0.431	26.129 ± 0.327	25.391 ± 0.702
BP(2,7)	118483	967.65	27.121 ± 0.550	26.172 ± 0.285	25.004 ± 0.564
FR(2,7)	118483	1061.41	27.205 ± 0.361	26.345 ± 0.301	25.635 ± 0.508
BP(3,7)	82163	967.23	27.345 ± 0.547	26.480 ± 0.292	25.495 ± 0.448
FR(3,7)	82163	1060.99	26.987 ± 0.509	26.406 ± 0.387	25.930 ± 0.395
BP(4,7)	69638	967.08	27.442 ± 0.331	26.691 ± 0.310	26.103 ± 0.282
FR(4,7)	69638	1060.85	27.539 ± 0.336	26.785 ± 0.468	26.055 ± 0.224
BP(5,7)	62858	967.01	27.343 ± 0.482	26.941 ± 0.353	26.513 ± 0.118
FR(5,7)	62858	1060.77	27.613 ± 0.184	26.819 ± 0.489	26.516 ± 0.529
BP(6,7)	1290	966.30	27.742 ± 0.225	27.518 ± 0.095	27.167 ± 0.116
FR(6,7)	1290	1060.06	27.610 ± 0.206	27.391 ± 0.090	27.129 ± 0.196

of the subsequent fully connected layers decreases. To further improve the performance of converged CNNs pretrained by BP, this section compares FR-PT with the BP-based post-training, both starting with the same pretrained baseline CNN. Each training configuration is repeated for 10 runs to obtain statistically reliable performance results.

For each layer index $l \in \{1, 2, \dots, L\}$ in the original well-trained baseline network, we freeze the weights and bias parameters of all subsequent layers after the l^{th} layer, and use algorithms described in Section 3 to generate the training datasets containing reconstructed feature maps \mathbf{a}_l^* for all instances, where the nearest embedding $\mathbf{a}_L^* = \mathbf{a}_L^{NE}$ is adopted in the optimal embedding part sending scalar labels to output vectors. These priorly obtained datasets are directly used to compute the reconstruction loss \mathcal{L}_{rec} (Eq. 2), as the parameters beyond the l_R^{th} layer remain frozen during post-training processes.

During each FR-PT process, the first l_S layers are frozen, indicating the total loss \mathcal{L} (Eq. 3) is used to optimize the parameters between the l_S^{th} layer and the l_R^{th} layer. FR-PT is evaluated across all possible hyperparameter combinations (l_S, l_R) for each baseline network architecture. The results are summarized in Tables 1-6 for each corresponding benchmark, including the number of trainable parameters, GPU memory usage (MB), and the mean and standard deviation of test accuracy (%).

It can be observed that FR-PT generally outperforms BP-PT when l_R is set to the last few layer indices, such as $l_R = 4$ for Cifar10 (Table 2); $l_R = 3, 4, 5$ for Cifar100 (Table 3); $l_R = 4, 5, 6$ for Tiny Imagenet (Table 4); $l_R = 6, 7$ for ImageNette (Table 5); $l_R = 5$ for ImageWoof (Table 6), whereas BP-PT surpasses FR-PT when l_R is set to the first few layer indices. The reason lies in the accumulation of information loss during the backward reverse computation, particularly due to reconstructions for pooling operations and convolutional operations with $C_l > C_{l+1}$. As a result, the reconstructed y^* -informed feature maps \mathbf{a}_l^* at the first few layers deviate significantly from the original forward-obtained ones $\hat{\mathbf{a}}_l$. This discrepancy leads to a larger violation of the pretrained parameters when optimizing the \mathcal{L}_{rec} term, thereby disturbing the training process. As for Mnist, note the test accuracy of FR-PT is relatively lower than that of BP-PT on Mnist (Table 1). This may be attributed to the baseline network not being fully converged, allowing the BP method to continue improving performance effectively. Nevertheless, it is FR-PT that achieves the highest post-training generalization performance on CIFAR-10, CIFAR-100, ImageNette, and ImageWoof.

It is evident that independently training a module requires less GPU memory compared to training the entire network. Moreover, the GPU memory usages of FR-PT are slightly higher than those of BP-PT under the same module from l_S to l_R , especially when l_R is small, due to the additional storage of reconstructed feature maps required by FR-PT.

In addition to training networks, the feature reconstruct technique can also be used to visualize how intermediate feature maps evolve as the model's capability improves. As shown in Fig. 4, the absolute values of $(\hat{\mathbf{a}}_l - \mathbf{a}_l^*)$ become progressively more blue as the test accuracy grows, suggesting the discrepancy gets smaller and the network generates true outputs more

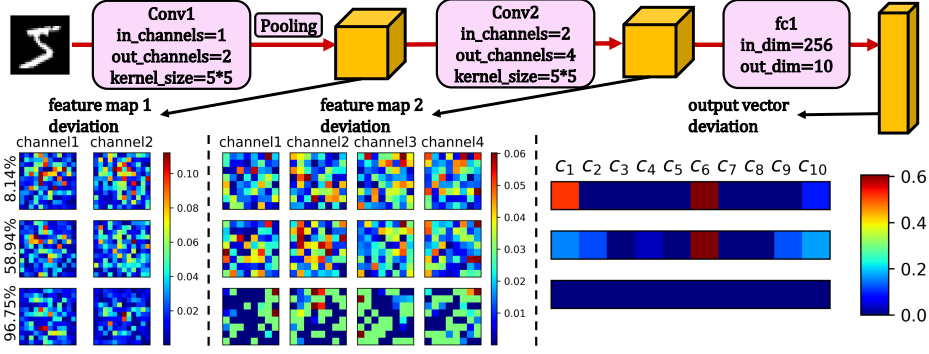


Figure 4: Absolute values of discrepancy between forward feature maps $\hat{\mathbf{a}}_l$ and reconstructed feature maps \mathbf{a}_l^* as a single CNN evolves on Mnist at three training stages with test accuracy being 8.14%, 58.94%, and 96.75%.

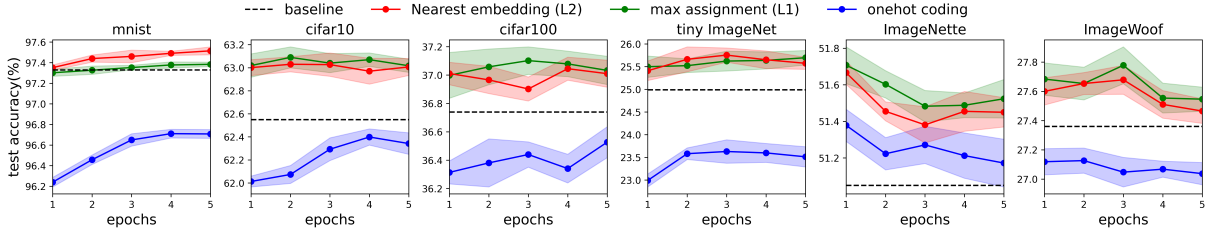


Figure 5: Average test accuracy with 95% confidence of optimal embedding approaches compared with one-hot coding across six benchmarks.

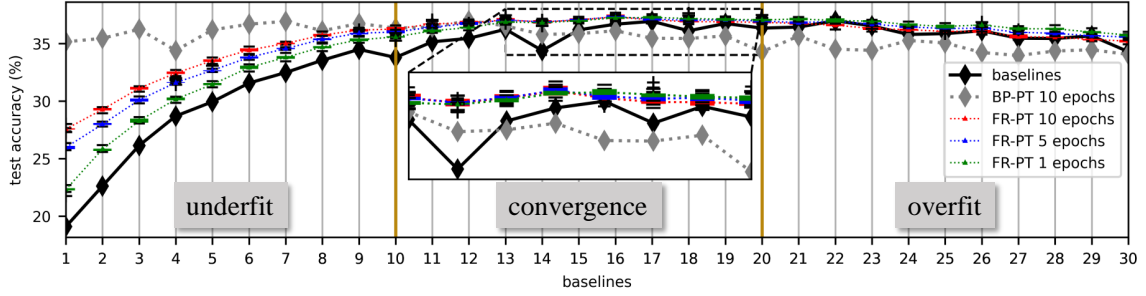


Figure 6: **The post-training results comparison across 30 baselines with different training stages.** A single baseline for Cifar100 evolves by one BP epoch per stage (black line). Then, for each post-training, only the parameters between 1th layer and 4th layer are trainable.

consistently. Besides, it can be observed that the regular strip-shaped characteristic in discrepancy’s distribution is waning gradually, leaving weak noises that largely caused by the reconstruction modeling error. This phenomenon strongly supports our insight that the consistency between input-informed and label-informed intermediate representations is intrinsically positively associated with the evaluation of the models.

4.2 Ablation Study on Optimal Embedding

As for the transform from a scalar label y^* to the output vector \mathbf{a}_L^* , we compared optimal embedding approaches \mathbf{a}_L^{MA} and \mathbf{a}_L^{NE} with the trivial one-hot code \mathbf{a}_L^{OH} of true label. The reconstruction loss is $\mathcal{L}_{rec} = L1Loss(\hat{\mathbf{a}}_L, \mathbf{a}_L^{MA})$, $\mathcal{L}_{rec} = MSE(\hat{\mathbf{a}}_L, \mathbf{a}_L^{NE})$ and $\mathcal{L}_{rec} = MSE(\hat{\mathbf{a}}_L, \mathbf{a}_L^{OH})$. The loss coefficient α is properly selected for each dataset. Only the last layer is trained during each post-training process to elimi-

nate confounding factors from other reconstruction processes.

As shown in Fig. 5, optimal embeddings outperform the one-hot approach across six benchmarks, indicating the effectiveness and indispensability of optimal embedding methods.

4.3 FR-PT on different training stages

This section explains why FR-based training is treated as a post-training approach in this study. A single CNN is pretrained by BP on Cifar100 for 30 epochs, where we save the model every epoch to obtain 30 baselines. The evolution of their test accuracies is depicted as the black line in Fig. 6. Each column is a post-training task on a specific baseline, where 10 epochs BP-PT (gray line), 1 epoch FR-PT (green box diagrams), 5 epochs FR-PT (blue box diagrams) and 10 epochs FR-PT (red box diagrams) are also demonstrated in Fig. 6.

It can be seen that FR-PT surpasses BP-PT when the

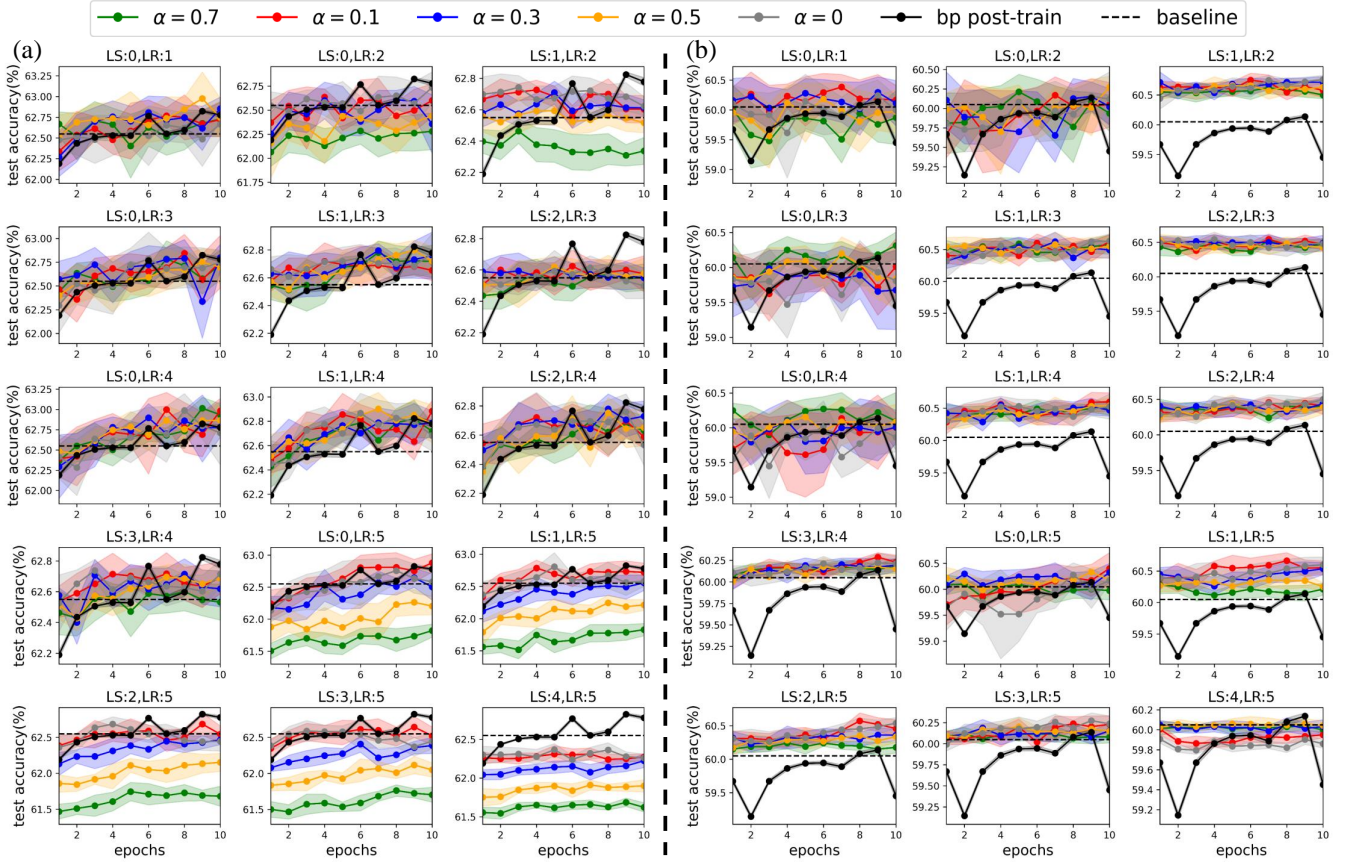


Figure 7: Influence comparison of FR-PT on different "3Conv+2fc" baselines of cifar10. (a) indicates the typical network architecture whose convolutional channel numbers increase in forward direction. (b) suggests a new architecture whose convolutional channel numbers decrease in forward direction.

baseline network just exhibit convergence. This may be explained that when baseline is underfitting, the BP approach still has dominant ability to improving networks, while the FR-PT does not gain good enough reconstructed feature maps due to the poor-quality parameters in the pre-matured networks. When baseline is overfitting, the whole network is entrapped in the local minimum and is difficult to escape.

Furthermore, "1 epoch FR-PT" becomes the best approach as the baseline convergence quality increases. The reason may be that the generalization of converged networks can not be further improved by iterative optimization logic, but by directly rectifying its prediction process to a more reasonable way.

4.4 FR-PT on different architectures

In Section 3, we separate feature reconstruction algorithms into two cases according to whether the neighboring layers' channel increases or decreases. To further study the difference about the influence on different network architectures, we perform FR-PT on cifar10, starting with two 3Conv+2fc baselines with different architectures. Type (a) has convolutional layers with 5, 10, and 15 channels sequentially, and the feature maps are reconstructed by solving least squares problems derived from the CCP, which means these reconstructed features do not satisfy the network computation perfectly. Type (b) has its convolutional layers with 15, 10, and 5 channels se-

quentially, and the feature maps are reconstructed by solving systems of linear equations by MDP, which means these reconstructed features perfectly satisfy network computation.

In Fig. 7, type (b) showcases more pronounced improvements of FR-PT over the BP post-training (black line), suggesting that feature reconstruction is more successful for architectures where the number of convolutional channels decreases in the forward direction.

5 Conclusion

This study presents a hierarchical and decoupled post-training framework based on feature reconstruction, applied on converged CNNs for image classification. A series of reverse computation algorithms is originally proposed, featuring rigorous theoretical foundations and high computational efficiency. Particularly noteworthy are the nearest embedding algorithm and the feature reconstruction for both linear and convolutional operations. Extensive experimental results statistically verify the effectiveness and rationality of the proposed framework.

Several potential research directions merit further exploration. First, the proposed feature reconstruction algorithms could be extended to other network architectures, such as Recurrent Neural Networks, ResNets, and Transformers, and applied to more sophisticated tasks. Second, integrating more

flexible and insightful techniques with feature reconstruction and optimal embedding represents a promising avenue for enhancing both interpretability and performance.

Acknowledgments

This work was supported by the National Key R&D Program of China, Project "Development of Large Model Technology and Scenario Library Construction for Autonomous Driving Data Closed-Loop" (Grant No. 2024YFB2505501).

References

- [1] Mohanad Abukmeil, Angelo Genovese, Vincenzo Piuri, Francesco Rundo, and Fabio Scotti. Towards explainable semantic segmentation for autonomous driving systems by multi-scale variational attention. In *2021 IEEE International Conference on Autonomous Systems (ICAS)*, pages 1–5, 2021.
- [2] Mayank Bansal, Alex Krizhevsky, and Abhijit S. Ogale. Chauffeurnet: Learning to drive by imitating the best and synthesizing the worst. *ArXiv*, abs/1812.03079, 2018.
- [3] Eugene Belilovsky, Michael Eickenberg, and Edouard Oyallon. Decoupled greedy learning of cnns. In *International Conference on Machine Learning*, pages 736–745. PMLR, 2020.
- [4] Mariusz Bojarski, Davide Del Testa, Daniel Dworakowski, Bernhard Firner, Beat Flepp, Praseoon Goyal, Lawrence D. Jackel, Mathew Monfort, Urs Muller, Jiakai Zhang, Xin Zhang, Jake Zhao, and Karol Zieba. End to end learning for self-driving cars, 2016.
- [5] Stephen Boyd and Lieven Vandenbergh. *Convex Optimization*. Cambridge University Press, 2004.
- [6] Nadia Burkart and Marco F. Huber. A survey on the explainability of supervised machine learning. *J. Artif. Int. Res.*, 70:245–317, May 2021.
- [7] Liang Gou, Lincan Zou, Nanxiang Li, Michael Hofmann, Arvind Kumar Shekar, Axel Wendt, and Liu Ren. Vatld: A visual analytics system to assess, understand and improve traffic light detection. *IEEE Transactions on Visualization and Computer Graphics*, 27(2):261–271, 2021.
- [8] Jyh-Jing Hwang, Runsheng Xu, Hubert Lin, Wei-Chih Hung, Jingwei Ji, Kristy Choi, Di Huang, Tong He, Paul Covington, Benjamin Sapp, Yin Zhou, James Guo, Dragomir Anguelov, and Mingxing Tan. Emma: End-to-end multimodal model for autonomous driving, 2024.
- [9] Max Jaderberg, Wojciech Marian Czarnecki, Simon Osindero, Oriol Vinyals, Alex Graves, David Silver, and Koray Kavukcuoglu. Decoupled neural interfaces using synthetic gradients, 2017.
- [10] Peng-Tao Jiang, Chang-Bin Zhang, Qibin Hou, Ming-Ming Cheng, and Yunchao Wei. Layercam: Exploring hierarchical class activation maps for localization. *IEEE Transactions on Image Processing*, 30:5875–5888, 2021.
- [11] Titong Jiang, Yahui Liu, Qing Dong, and Tao Xu. Intention-aware interactive transformer for real-time vehicle trajectory prediction in dense traffic. *Transportation Research Record*, 2677(3):946–960, 2023.
- [12] Peter Karkus, Boris Ivanovic, Shie Mannor, and Marco Pavone. Diffstack: A differentiable and modular control stack for autonomous vehicles. In Karen Liu, Dana Kulic, and Jeff Ichnowski, editors, *Proceedings of The 6th Conference on Robot Learning*, volume 205 of *Proceedings of Machine Learning Research*, pages 2170–2180. PMLR, 14–18 Dec 2023.
- [13] Youngseok Kim, Sanmin Kim, Sangmin Sim, Jun Won Choi, and Dongsuk Kum. Boosting monocular 3d object detection with object-centric auxiliary depth supervision. *IEEE Transactions on Intelligent Transportation Systems*, 24(2):1801–1813, 2023.
- [14] Pawit Kochakarn, Daniele De Martini, Daniel Omeiza, and Lars Kunze. Explainable action prediction through self-supervision on scene graphs. In *2023 IEEE International Conference on Robotics and Automation (ICRA)*, pages 1479–1485, 2023.
- [15] Suresh Kolekar, Shilpa Gite, Biswajeet Pradhan, and Abdullah Alamri. Explainable ai in scene understanding for autonomous vehicles in unstructured traffic environments on indian roads using the inception u-net model with grad-cam visualization. *Sensors*, 22(24), 2022.
- [16] Anton Kuznietsov, Balint Gyevar, Cheng Wang, Steven Peters, and Stefano V. Albrecht. Explainable ai for safe and trustworthy autonomous driving: A systematic review. *IEEE Transactions on Intelligent Transportation Systems*, 25(12):19342–19364, 2024.
- [17] Shichao Li, Zengqiang Yan, Hongyang Li, and Kwang-Ting Cheng. Exploring intermediate representation for monocular vehicle pose estimation. In *Proceedings of the IEEE/CVF Conference on Computer Vision and Pattern Recognition (CVPR)*, pages 1873–1883, June 2021.
- [18] Harsh Mankodiya, Dhairya Jadav, Rajesh Gupta, Sudeep Tanwar, Wei-Chiang Hong, and Ravi Sharma. Od-xai: Explainable ai-based semantic object detection for autonomous vehicles. *Applied Sciences*, 12(11), 2022.
- [19] Amitha Mathew, P Amudha, and S Sivakumari. Deep learning techniques: an overview. *Advanced Machine Learning Technologies and Applications: Proceedings of AMLTA 2020*, pages 599–608, 2021.
- [20] Simon Odense and Artur d’Avila Garcez. Layerwise knowledge extraction from deep convolutional networks. *arXiv preprint arXiv:2003.09000*, 2020.

- [21] Chenbin Pan, Burhaneddin Yaman, Senem Velipasalar, and Liu Ren. Clip-bevformer: Enhancing multi-view image-based bev detector with ground truth flow, 2024.
- [22] Jiawei Peng, Yicheng Xu, Zhiping Lin, Zhenyu Weng, Zishuo Yang, and Huiping Zhuang. Decoupled neural network training with re-computation and weight prediction. *PloS one*, 18(2):e0276427, 2023.
- [23] David Schinagl, Georg Krispel, Horst Possegger, Peter M. Roth, and Horst Bischof. Occam’s laser: Occlusion-based attribution maps for 3d object detectors on lidar data. In *Proceedings of the IEEE/CVF Conference on Computer Vision and Pattern Recognition (CVPR)*, pages 1141–1150, June 2022.
- [24] David Schinagl, Georg Krispel, Horst Possegger, Peter M. Roth, and Horst Bischof. Occam’s laser: Occlusion-based attribution maps for 3d object detectors on lidar data. In *2022 IEEE/CVF Conference on Computer Vision and Pattern Recognition (CVPR)*, pages 1131–1140, 2022.
- [25] Ramprasaath R. Selvaraju, Michael Cogswell, Abhishek Das, Ramakrishna Vedantam, Devi Parikh, and Dhruv Batra. Grad-cam: Visual explanations from deep networks via gradient-based localization. In *2017 IEEE International Conference on Computer Vision (ICCV)*, pages 618–626, 2017.
- [26] Karen Simonyan, Andrea Vedaldi, and Andrew Zisserman. Deep inside convolutional networks: Visualising image classification models and saliency maps. *CoRR*, abs/1312.6034, 2013.
- [27] Ardi Tampuu, Tambet Matiisen, Maksym Semikin, Dmytro Fishman, and Naveed Muhammad. A survey of end-to-end driving: Architectures and training methods. *IEEE Transactions on Neural Networks and Learning Systems*, 33(4):1364–1384, 2022.
- [28] Kai Wang, Jie Hou, and Xianlin Zeng. Lane-change intention prediction of surrounding vehicles using bilstm-crf models with rule embedding. In *2022 China Automation Congress (CAC)*, pages 2764–2769, 2022.
- [29] Shaobo Wang, Yicun Yang, Zhiyuan Liu, Chenghao Sun, Xuming Hu, Conghui He, and Linfeng Zhang. Dataset distillation with neural characteristic function: A minmax perspective, 2025.
- [30] Zhenhua Xu, Yujia Zhang, Enze Xie, Zhen Zhao, Yong Guo, Kwan-Yee K. Wong, Zhenguo Li, and Hengshuang Zhao. Drivegpt4: Interpretable end-to-end autonomous driving via large language model. *IEEE Robotics and Automation Letters*, 9(10):8186–8193, 2024.
- [31] Chenyu Yang, Yuntao Chen, Hao Tian, Chenxin Tao, Xizhou Zhu, Zhaoxiang Zhang, Gao Huang, Hongyang Li, Yu Qiao, Lewei Lu, Jie Zhou, and Jifeng Dai. Bevformer v2: Adapting modern image backbones to bird’s-eye-view recognition via perspective supervision. In *Proceedings of the IEEE/CVF Conference on Computer Vision and Pattern Recognition (CVPR)*, pages 17830–17839, June 2023.
- [32] Hakan Yekta Yatbaz, Mehrdad Dianati, and Roger Woodman. Introspection of dnn-based perception functions in automated driving systems: State-of-the-art and open research challenges. *IEEE Transactions on Intelligent Transportation Systems*, 25(2):1112–1130, 2024.
- [33] Keisuke Yoneda, Naoki Ichihara, Hotsuyuki Kawanishi, Tadashi Okuno, Lu Cao, and Naoki Suganuma. Sun-glare region recognition using visual explanations for traffic light detection. In *2021 IEEE Intelligent Vehicles Symposium (IV)*, pages 1464–1469, 2021.
- [34] Jason Yosinski, Jeff Clune, Anh Nguyen, Thomas Fuchs, and Hod Lipson. Understanding neural networks through deep visualization, 2015.
- [35] Matthew D Zeiler and Rob Fergus. Visualizing and understanding convolutional networks, 2013.
- [36] Ludan Zhang, Chaoyi Chen, Lei He, and Keqiang Li. Feature map convergence evaluation for functional module, 2024.
- [37] Quan Zheng, Ziwei Wang, Jie Zhou, and Jiwen Lu. Shapcam: Visual explanations for convolutional neural networks based on shapley value. In *European conference on computer vision*, pages 459–474. Springer, 2022.
- [38] Wenzhao Zheng, Ruiqi Song, Xianda Guo, Chenming Zhang, and Long Chen. Genad: Generative end-to-end autonomous driving. In *European Conference on Computer Vision*, pages 87–104. Springer, 2024.
- [39] Bolei Zhou, Aditya Khosla, Agata Lapedriza, Aude Oliva, and Antonio Torralba. Learning deep features for discriminative localization. In *2016 IEEE Conference on Computer Vision and Pattern Recognition (CVPR)*, pages 2921–2929, 2016.
- [40] Huiping Zhuang, Yi Wang, Qinglai Liu, and Zhiping Lin. Fully decoupled neural network learning using delayed gradients. *IEEE transactions on neural networks and learning systems*, 33(10):6013–6020, 2021.